# A Novel Multiphysics Multiscale Multiporosity Shale Gas Transport Model for Geomechanics/Flow Coupling in Steady and Transient States

**Zihao Li, Yuntian Teng, Ming Fan, Nino Ripepi,** and **Cheng Chen*,** Virginia Tech

## Summary

A novel multiphysics multiscale multiporosity shale gas transport ($M^3ST$) model was developed to investigate shale gas transport in both transient and steady states. The microscale model component contains a kerogen domain and an inorganic matrix domain, and each domain has its own geomechanical and gas transport properties. Permeabilities of various shale cores were measured in the laboratory using a pulse decay permeameter (PDP) with different pore pressure and confining stress combinations. The PDP-measured apparent permeability as a function of pore pressure under two effective stresses was fitted using the microscale $M^3ST$ model component based on nonlinear least squares fitting (NLSF), and the fitted model parameters were able to provide accurate model predictions for another effective stress. The parameters and petrophysical properties determined in the steady state were then used in the transient-state, continuum-scale $M^3ST$ model component, which performed history matching of the evolutions of the upstream and downstream gas pressures. In addition, a double-exponential empirical model was developed as a powerful alternative to the $M^3ST$ model to fit laboratory-measured apparent permeability under various effective stresses and pore pressures. The developed $M^3ST$ model and the research findings in this study provided critical insights into the role of the multiphysics mechanisms, including geomechanics, fluid dynamics and transport, and the Klinkenberg effect on shale gas transport across different spatial scales in both steady and transient states.

Key Points:

- An $M^3ST$ model accounts for the coupling of geomechanics and gas transport in shale.
- Microscale parameters fitted to laboratory data lead to successful history matching of gas pressure evolutions at the core scale.
- A double-exponential empirical model successfully describes apparent permeability changes under various effective stress and pore pressure.

## Introduction and Background

Production of hydrocarbon energy resources from shale, a fine-grained, low-permeability geological formation, has changed the global energy outlook. Recovery of shale oil and gas has become economically viable due to the development of hydraulic fracturing and horizontal drilling (Montgomery and Smith 2010; Chen et al. 2013; Gu and Mohanty 2014; Stringfellow et al. 2014; Wang et al. 2018). Compared with conventional enhanced oil and gas recovery (Li et al. 2016b; Wang et al. 2017; Zhao et al. 2017; Tang et al. 2019), unconventional resource development is generally associated with a wide range of benefits such as job growth and improved infrastructure and municipal developments.

Extensive research on the correlation between effective stress and shale permeability has been conducted using both laboratory experiments and analytical models (Akkutlu and Fathi 2012; Alnoaimi and Kovscek 2013; Mehmani et al. 2013; Heller et al. 2014; Chen 2016; Ghanbarian and Javadpour 2017; Guo et al. 2018; Sheng et al. 2018; Wang et al. 2019; Zhang et al. 2021). It is generally expected that the permeability of a shale formation decreases with increasing effective stress due to compressed pore space and closure of microscale fractures. In addition to effective stress, the apparent (i.e., measured) permeability of a shale formation depends on the pore pressure if the testing fluid is a gas. This phenomenon is caused by nanoscale pores in shale and is referred to as the Klinkenberg effect. In 1941, Klinkenberg developed the gas slippage theory (i.e., the Klinkenberg effect) to explain the enhancement of measured apparent permeability for gas flow in nanopores (Klinkenberg 1941). The Klinkenberg effect occurs when the mean-free path of the measured gas molecules is longer than the diameter of the nanopore through which they travel. Consequently, gas molecules collide with the pore walls more frequently than with one another, leading to Knudsen diffusion that causes a slip-velocity boundary condition on the pore walls, which enhances the apparent permeability of the nanopore. Therefore, the Klinkenberg effect has a critical impact on gas flow in porous media having ultralow permeability (Wu et al. 1998). Although the Klinkenberg effect may not influence the apparent permeability under in-situ high reservoir pressures (Civan 2020), it plays an important role in the interpretation of laboratory measurements because pore pressures used in laboratory experiments can be at the levels where the Klinkenberg effect is noticeable (Soeder 1988; Li et al. 2020).

The Knudson number (Kn) is an important dimensionless number relevant to the Klinkenberg effect. Kn is calculated as the ratio of the gas mean-free-path length $\lambda$ to the effective pore width $h$. The Navier-Stokes equations can be used to describe gas flow with a no-slip boundary condition on the pore walls when Kn is smaller than 0.001. When the Kn is increased to the range between 0.001 and 0.1, the gas flow is in the slip flow regime in which the noncontinuum effect at the solid/fluid boundary can be accounted for using a velocity slip on the pore walls; the Navier-Stokes equations can still be used to describe the bulk gas flow (Beskok and Karniadakis 1999). The continuous increase of Kn into the range between 0.1 and 10 will lead to the transitional flow regime, followed by the free molecular flow regime when Kn is larger than 10, in which the Navier-Stokes equations cannot be used to describe gas flow in the pores (Tian et al. 2019).

Because of the important implication of the Klinkenberg effect to shale gas transport, a variety of analytical approaches have been developed to describe gas flow subjected to the Klinkenberg effect in tight porous media (Wu et al. 1998; Innocentini and Pandolfelli

*Corresponding author; now with Stevens Institute of Technology; email: cchen6@stevens.edu



Original SPE manuscript received for review 21 January 2021. Revised manuscript received for review 7 June 2021. Paper (SPE 206726) peer approved 10 June 2021.

2001; Zhu et al. 2007; Hu et al. 2009; Hayek 2015; Li et al. 2019, 2020; Yuan et al. 2020). In addition, many studies have been conducted to investigate the Klinkenberg effect and its role on multiphase flow (Blanchard et al. 2007), the dynamic Klinkenberg coefficient (Wang et al. 2014), and fractal theory (Li et al. 2016a). All these studies confirmed that the permeability of tight reservoir rocks depends closely on effective stress and the Klinkenberg effect.

Despite numerous previous studies on the relationship between shale's apparent permeability, effective stress, and pore pressure, a mechanistic model is still needed to adequately describe the multiphysics multiscale processes that regulate shale gas transport in tight formations. The lack of such a mechanistic, theoretical model was due to several challenges. First, the model needs to have a multiporosity geometry to differentiate kerogen (i.e., organic matter) and inorganic matrix at the microscopic scale (Chen 2016), because it is the nanopores in kerogen that cause the Klinkenberg effect in shale. Second, the model needs to account for multiphysics mechanisms, including geomechanics, fluid flow and transport, and the Klinkenberg effect, because the effective stress and pore pressure in a shale gas reservoir influence the apparent permeability of the formation through these multiphysics mechanisms. Third, the model should be multiscale and also reasonably simple so that it can be easily calibrated by laboratory core permeability measurements and upscaled to history match continuum-scale pore pressure evolutions. To solve these challenges, in this study, a novel $M^3ST$ model was developed to describe shale gas transport in both transient and steady states, which provides mechanistic insight into the dependence of shale's apparent permeability on effective stress and pore pressure.

## Overview of the Experimental/Modeling Approaches

This section provides an overview of the experimental and modeling approaches used in this paper, including the details for the principle of a pressure PDP and how it measures shale core permeability and the upstream and downstream gas pressure evolutions in the transient state. The section Determination of the Biot's Coefficient introduces basic theories of the Biot's coefficient and Klinkenberg effect, which are relevant to the role of effective stress and pore pressure, respectively, on shale's apparent permeability. The section $M^3ST$ Model develops a novel $M^3ST$ model to study gas transport in shale in both transient and steady states. Particularly, the microscale $M^3ST$ model component was used to fit PDP measurements of shale permeability based on NLSF to determine critical model parameters; the fitted model parameters were used to predict shale permeability under other effective stresses and then imported into the macroscale component of the $M^3ST$ model to history match continuum-scale gas pressure evolutions measured by the PDP. The section A Novel Double-Exponential Empirical Model derives a double-exponential empirical model to describe the dependence of shale's apparent permeability on effective stress and pore pressure. The section Results and Discussion provides experimental and modeling results as well as discussions and implications.

**Fig. 1** illustrates the Eagle Ford and Mancos shale cores used in this study. The two Eagle Ford cores were marked as "Eagle Ford 1A" and "Eagle Ford 1B," and the two Mancos cores were marked as "Mancos 1A" and "Mancos 1B." The cores were 2-in. in length and 1 in. in diameter. The bedding plane direction was parallel to the core axis direction. The total organic carbon contents were 2.02 and 1.37%, respectively, for the Eagle Ford and Mancos cores.

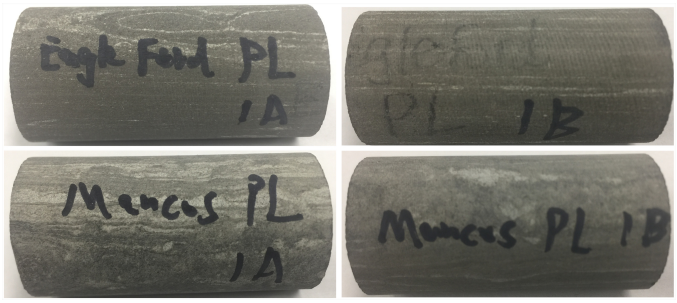


**Fig. 1—Two Eagle Ford shale core plugs (top row) and two Mancos shale core plugs (bottom row) for the PDP permeability measurements. The shale core plugs were 2 in. in length and 1 in. in diameter. The shale bedding plane direction was parallel to the core plug axis direction.**

**Fig. 2** illustrates a schematic plot of the PDP equipment setup, which provides a convenient and dynamic approach for measuring the apparent permeability of tight rocks (Jones 1997). First, with the fill valve and Valves 1 through 4 opened, all the gas reservoirs are filled to the desired starting pressure. The upstream reservoir volume $V_1$ and downstream reservoir volume $V_2$ are both 10 $cm^3$. Next, the fill valve is closed, and after a period of soaking time (usually 300 seconds) Valve 2 is closed. Gas in the downstream reservoir $V_2$ will then be released through the needle valve and shut-off valve to obtain a pressure lower than the upstream reservoir pressure, which is referred to as the differential pressure $\Delta P$. When $\Delta P$ stabilizes, Valves 3 and 4 are both closed. Gas molecules will gradually penetrate through the core sample to migrate from the upstream reservoir to the downstream reservoir, leading to continuously decreasing upstream reservoir pressure and increasing downstream reservoir pressure. In this process, the differential pressure $\Delta P$ continuously decays. The higher the permeability of the core plug, the faster the decay of $\Delta P$. The permeability of the core plug can then be calculated based on the decay rate of $\Delta P$ following the standard procedure of PDP analysis (Dicker and Smits 1988; Jones 1997).

## Determination of the Biot's Coefficient

During the recovery of unconventional hydrocarbon resources, increased effective stress can cause rock matrix deformation, which plays a vital role on the petrophysical properties of the shale formation during production, including permeability (Fan et al. 2018, 2021b), wettability (Guo et al. 2020), and fluid phase behavior (Zhao et al. 2021). Based on the poroelasticity theory from Biot (1941), a porous medium's deformation influences the fluid flow and vice versa. The Biot's coefficient (i.e., Biot's poroelastic term) is a critical concept for the effective stress calculation in a porous medium, which represents the fluid volume change induced by bulk volume changes in the drained condition (Müller and Sahay 2016). The calculation of Biot's coefficient can be based on various correlations, and Civan (2021) summarized these equations used in the literature, which include linear, power-law, exponential, inverse, logarithmic,

and modified power-law correlations. According to Terzaghi et al. (1996), the pore pressure of the fluid reduces the effective stress in a rock mineral matrix, and Biot's coefficient describes the reduction of effective stress quantitatively (Bernabe 1986):

$$P_e = P_c - \chi P_p, \quad \ldots\ldots (1)$$

where $\chi$ is Biot's coefficient; and $P_e$, $P_c$, and $P_p$ are effective stress, confining pressure, and pore pressure, respectively. Previous studies (Warpinski and Teufel 1992; Cheng 1997; Lee 2002; Ojala and Fjær 2007; Tan and Konietzky 2014; Selvadurai 2019) have used both laboratory experiments and theoretical methods to estimate the $\chi$ value in a certain type of rock.

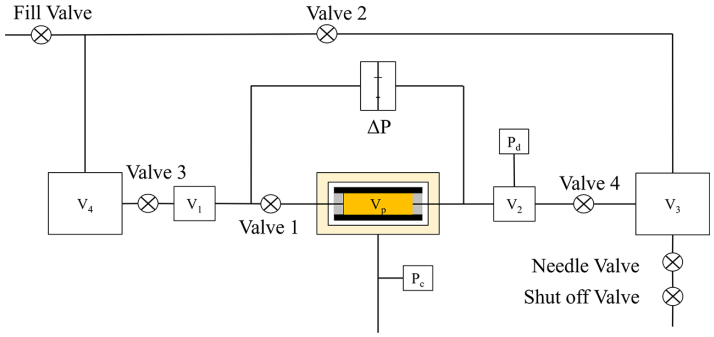


**Fig. 2—Schematic PDP equipment setup, which consists of an upstream gas reservoir having a volume of $V_1$, a high-strength core holder that contains the core sample having a pore volume (PV) of $V_p$, a downstream gas reservoir having a volume of $V_2$, two large gas reservoirs $V_3$ and $V_4$ that stabilize the initial gas pressures in $V_1$ and $V_2$, a differential pressure transducer to continuously measure the differential pressure, $\Delta P$, and a pressure transducer to measure the downstream reservoir pressure, $P_d$. This diagram was modified from the CoreLaboratories, Inc. PDP-200 operation manual.**

In this study, we used the PDP to measure shale's apparent permeability under various pore pressures and confining pressures to calculate the Biot's coefficient based on Geertsma (1957), Kwon et al. (2001), and Civan (2021). Because the apparent permeability $k_a$ depends on both $P_p$ and $P_c$, we express $k_a$ as a function of these two independent variables:

$$k_a = k_a(P_c, P_p), \quad \ldots\ldots (2)$$

Because the permeability of natural geologic formations in general follows a lognormal distribution (Chen and Zeng 2015), we make a logarithm transformation for Eq. 2 and obtain

$$\log(k_a) = \log[k_a(P_c, P_p)]. \quad \ldots\ldots (3)$$

Taking the differential of Eq. 3 leads to

$$\mathrm{d}\log(k_a) = \left(\frac{\partial \log(k_a)}{\partial P_c}\right)\mathrm{d}P_c + \left(\frac{\partial \log(k_a)}{\partial P_p}\right)\mathrm{d}P_p. \quad \ldots\ldots (4)$$

Similarly, taking the differential of Eq. 1 leads to:

$$\mathrm{d}P_e = \mathrm{d}P_c - \chi \mathrm{d}P_p. \quad \ldots\ldots (5)$$

When the pore pressure is sufficiently high, the Klinkenberg effect is inhibited; in this scenario, the apparent permeability is equal to the absolute permeability, which depends only on the pore geometry that is controlled by the effective stress. Therefore, when the change of effective stress $\mathrm{d}P_e$ is zero, the change of apparent permeability $\mathrm{d}\log(k_a)$ is also zero. Therefore, Eqs. 4 and 5 lead to

$$0 = \left(\frac{\partial \log(k_a)}{\partial P_c}\right)\mathrm{d}P_c + \left(\frac{\partial \log(k_a)}{\partial P_p}\right)\mathrm{d}P_p, \quad \ldots\ldots (6)$$

and

$$0 = \mathrm{d}P_c - \chi \mathrm{d}P_p. \quad \ldots\ldots (7)$$

Combining Eqs. 6 and 7, one can solve for the Biot's coefficient $\chi$ as follows:

$$\chi = -\left(\frac{\partial \log(k_a)}{\partial P_p}\right) \Big/ \left(\frac{\partial \log(k_a)}{\partial P_c}\right). \quad \ldots\ldots (8)$$

The Klinkenberg effect) was introduced to explain the difference between measured permeability (i.e., apparent permeability) and absolute permeability in tight rocks. The Klinkenberg coefficient $b$ was applied to quantify the influence of pore pressure and nanopore size on the measured apparent permeability:

$$\frac{k_a}{k} = 1 + \frac{b}{P_p}, \quad \ldots\ldots (9)$$

where $k_a$ and $k$ are apparent permeability (m$^2$) and absolute permeability (m$^2$), respectively, and $b$ is the Klinkenberg coefficient (Pa). The Klinkenberg coefficient depends on the rock's petrophysical properties and can be determined based on the analysis of the mass fluxes contributed by the Knudsen diffusion and viscous flow. The value of $b$ in a planar nanopore can be expressed as (Chen 2016; Li et al. 2020):

$$b = \frac{2\mu}{h}\left(\frac{2}{\alpha} - 1\right)\sqrt{\frac{8\pi RT}{M}} + \frac{4\mu}{h}\sqrt{\frac{8RT}{\pi M}}, \qquad (10)$$

where $\mu$ is dynamic viscosity (Pa·s); $\alpha$ is the tangential momentum accommodation coefficient with a value from 0 to 1; $R$ is the gas constant and equal to 8.314 J/mol/K; $T$ is the absolute temperature (K); $M$ is the molar mass (kg/mol); and $h$ is the effective pore width (m). Details of the derivation of Eq. 10 can be found in one of our previous studies (Li et al. 2020). Based on Eq. 10, it is clear the value of $b$ is inversely proportional to the effective pore width $h$, which explains why the Klinkenberg effect is more significant in tight rocks where the pore size is in general small.

## M$^3$ST Model

**Fig. 3** illustrates the microscale and macroscale geometric models for shale gas transport, which is based on the extension of the multiphysics shale gas transport model published in our previous study (Li et al. 2020). This model forms the microscale component of the M$^3$ST model and is in the 2D space, which consists of two domains for shale gas transport: the organic domain (kerogen) and the inorganic matrix. Each domain has its respective geomechanical compressibility, pore width, porosity, and permeability. Because of the high mass flux contributed by viscous flow, we ignore molecular diffusion and adsorption and desorption in the inorganic matrix (Chen 2016). Therefore, the microscale M$^3$ST model characterizes gas transport in the kerogen and inorganic matrix separately. The entire shale sample is subjected to compressive stress because of the external confining pressure, which regulates the pore sizes in both the kerogen and inorganic matrix.

**Fig. 3—2D schematic picture of the microscale and macroscale M$^3$ST model components.**

The absolute permeability of a pore in the 2D space can be calculated as

$$k = \frac{h^2}{12}, \qquad (11)$$

where $k$ is absolute permeability (m$^2$), and $h$ is pore width (m). Combining Eq. 2 with Eq. 11, one obtains

$$\begin{aligned} k_{ai} &= \frac{h_i{}^2}{12}\left(1 + \frac{b_i}{P_p}\right) \\ k_{ak} &= \frac{h_k{}^2}{12}\left(1 + \frac{b_k}{P_p}\right), \end{aligned} \qquad (12)$$

where $k_{ai}$ and $k_{ak}$ are the apparent permeabilities in the inorganic matrix and kerogen, respectively; $h_i$ and $h_k$ are pore widths in the inorganic matrix and kerogen, respectively; and $b_i$ and $b_k$ are the Klinkenberg coefficients in the inorganic matrix and kerogen, respectively. The apparent permeability of the entire domain, including both the inorganic matrix and the kerogen, is calculated based on Darcy's law:

$$\overline{k_a} = \frac{(Q_i + Q_k)\mu}{A \cdot \nabla P_p}, \qquad (13)$$

where $A$ is total cross-sectional area (m$^2$), $\mu$ is dynamic viscosity (Pa·s), $\nabla P_p$ is pressure gradient through the pore (Pa/m), and $Q_i$ and $Q_k$ are the flow rates in the inorganic matrix and the kerogen domain, respectively. Specifically, the total cross-sectional area $A$, the kerogen cross-sectional area $A_k$, and the inorganic matrix cross-sectional area $A_i$ can be calculated, respectively, as

$$\begin{aligned} A &= \frac{h_i + N \cdot h_k}{\phi} \\ A_i &= h_i + (1 - \varepsilon_{ks}) \cdot S \\ A_k &= N \cdot h_k + \varepsilon_{ks} \cdot S, \end{aligned} \qquad (14)$$

where $\phi$ is the total porosity that accounts for both kerogen and inorganic pores; $N$ is the number of kerogen pores per inorganic pore; $S$ is the solid cross-sectional area associated with one inorganic pore; and $\varepsilon_{ks}$ is kerogen solid volume per unit total solid volume and can be determined using the total organic carbon content. Based on Darcy's law and Eq. 12, $Q_i$ and $Q_k$ can be calculated as

$$Q_i = \frac{k_{ai}}{\mu} \cdot \nabla P_p \cdot h_i = \frac{{h_i}^3}{12} \cdot \frac{\nabla P_p}{\mu} \left(1 + \frac{b_i}{P_p}\right)$$
$$Q_k = N \cdot \frac{k_{ak}}{\mu} \cdot \nabla P_p \cdot h_k = N \cdot \frac{{h_k}^3}{12} \cdot \frac{\nabla P_p}{\mu} \left(1 + \frac{b_k}{P_p}\right). \quad \ldots\ldots (15)$$

In Eq. 15, the Klinkenberg coefficients $b_i$ and $b_k$ are calculated based on Eq. 10:

$$b_i = \frac{2\mu}{h_i}\left(\frac{2}{\alpha} - 1\right)\sqrt{\frac{8\pi RT}{M}} + \frac{4\mu}{h_i}\sqrt{\frac{8RT}{\pi M}}$$
$$b_k = \frac{2\mu}{h_k}\left(\frac{2}{\alpha} - 1\right)\sqrt{\frac{8\pi RT}{M}} + \frac{4\mu}{h_k}\sqrt{\frac{8RT}{\pi M}}. \quad \ldots\ldots (16)$$

The pore widths in Eq. 15 are subject to the effective stress and calculated as

$$h_i = h_{i0}(1 - \beta_i P_e)$$
$$h_k = h_{k0}(1 - \beta_k P_e), \quad \ldots\ldots (17)$$

where $h_{i0}$ and $h_{k0}$ are the initial (i.e., reference) pore widths in the inorganic matrix and kerogen domain, respectively; $P_e$ is the effective stress and calculated as $P_e = P_c - \chi P_p$; and $\beta_i$ and $\beta_k$ are the isothermal compressibility coefficients for pore width in the inorganic matrix and kerogen domain, respectively, which describe pore width's responses to the change of effective stress.

In Eq. 14, the total porosity $\phi$ can be calculated as

$$\phi = \frac{h_i + Nh_k}{h_i + Nh_k + S} = \frac{h_{i0}(1 - \beta_i P_e) + Nh_{k0}(1 - \beta_k P_e)}{h_{i0}(1 - \beta_i P_e) + Nh_{k0}(1 - \beta_k P_e) + S}. \quad \ldots\ldots (18)$$

Plugging Eqs. 14–18 into Eq. 13, one can rewrite Eq. 13 as:

$$\overline{k_a} = \frac{[h_{i0}(1 - \beta_i P_e)]^3 \left[1 + \frac{2\mu\left(\frac{2}{\alpha} - 1\right)\sqrt{\frac{8\pi RT}{M}} + 4\mu\sqrt{\frac{8RT}{\pi M}}}{h_{i0}(1 - \beta_i P_e)P_p}\right] + N \cdot [h_{k0}(1 - \beta_k P_e)]^3 \left[1 + \frac{2\mu\left(\frac{2}{\alpha} - 1\right)\sqrt{\frac{8\pi RT}{M}} + 4\mu\sqrt{\frac{8RT}{\pi M}}}{h_{k0}(1 - \beta_k P_e)P_p}\right]}{12[h_{i0}(1 - \beta_i P_e) + N \cdot h_{k0}(1 - \beta_k P_e) + S]}. \quad \ldots\ldots (19)$$

Eq. 19 is the microscale component of the M$^3$ST model based on our previous work (Li et al. 2020) for predicting the overall apparent permeability $\overline{k_a}$ for a shale sample that consists of an inorganic matrix and a kerogen domain. This model takes two independent input variables on the right-hand side of Eq. 19, which are the effective stress $P_e$ and the pore pressure $P_p$.

Using the same approach, one can calculate the apparent permeabilities of the inorganic matrix and kerogen domain as follows:

$$k_{ai} = \frac{[h_{i0}(1 - \beta_i P_e)]^3}{12[h_{i0}(1 - \beta_i P_e) + (1 - \varepsilon_{ks}) \cdot S]} \cdot \left[1 + \frac{2\mu\left(\frac{2}{\alpha} - 1\right)\sqrt{\frac{8\pi RT}{M}} + 4\mu\sqrt{\frac{8RT}{\pi M}}}{h_{i0}(1 - \beta_i P_e)P_p}\right]$$
$$k_{ak} = \frac{N \cdot [h_{k0}(1 - \beta_k P_e)]^3}{12[N \cdot h_{k0}(1 - \beta_k P_e) + \varepsilon_{ks} \cdot S]} \cdot \left[1 + \frac{2\mu\left(\frac{2}{\alpha} - 1\right)\sqrt{\frac{8\pi RT}{M}} + 4\mu\sqrt{\frac{8RT}{\pi M}}}{h_{k0}(1 - \beta_k P_e)P_p}\right]. \quad \ldots\ldots (20)$$

Similarly, these two equations take $P_e$ and $P_p$ as model inputs on the right-hand side. The model outputs are the inorganic matrix apparent permeability $k_{ai}$ and kerogen apparent permeability $k_{ak}$ separately.

The parameters in the microscale M$^3$ST model component (Eq. 19) were determined through PDP data fitting and then plugged into Eq. 20 to determine $k_{ai}$ and $k_{ak}$, which were then used in the continuum-scale M$^3$ST model component (Eqs. 21 through 23) to simulate the transient-state pressure evolutions at the larger (inch) scale. Particularly, the continuum-scale M$^3$ST model component is based on the fully coupled, two-porosity transport model published in our previous study (Chen 2016), and gas transport processes in the kerogen domain and inorganic matrix are described by Eqs. 21 and 22, respectively:

$$\varepsilon_{kp}\phi\frac{\partial C_k}{\partial t} + \varepsilon_{ks}(1 - \phi)\frac{\partial C_\mu}{\partial t} = \frac{\partial}{\partial x}\left[zRTC_k\frac{k_{ak}}{\mu}\frac{\partial C_k}{\partial x}\right] + \Gamma, \quad \ldots\ldots (21)$$
$$(1 - \varepsilon_{kp})\phi\frac{\partial C_i}{\partial t} = \frac{\partial}{\partial x}\left[zRTC_i\frac{k_{ai}}{\mu}\frac{\partial C_i}{\partial x}\right] - \Gamma, \quad \ldots\ldots (22)$$

where $\varepsilon_{kp}$ is kerogen PV per unit total PV and can be written as $\varepsilon_{kp} = (N \cdot h_{k0})/(N \cdot h_{k0} + h_{i0})$; $C_k$ and $C_i$ are the molar concentrations of free gas within the kerogen and inorganic matrix in the unit of moles per kerogen PV and inorganic PV, respectively (mol/m$^3$); $C_\mu$ is adsorbed gas molar concentration within kerogen in the unit of moles per kerogen solid volume (mol/m$^3$); $\phi$ is the total porosity accounting for interconnected pores within both kerogen and inorganic matrix; $x$ is the distance in the longitudinal direction (m); $t$ is time (seconds); $z$ is the compressibility factor; $\Gamma$ is the mass transfer rate between kerogen and inorganic matrix (mol/m$^3$/s), which can be written as $\Gamma = m(C_i - C_k)$, where $m$ is the mass exchange rate coefficient (1/seconds). Based on the Langmuir adsorption model, the mass exchange in the kerogen domain between adsorbed gas and free gas can be expressed as

$$\frac{\partial C_\mu}{\partial t} = K_{\mathrm{des}}\left[K(C_{\mu\max} - C_\mu)C_k - C_\mu\right], \quad (23)$$

where $C_{\mu\max}$ is the maximum monolayer adsorption concentration of gas in the kerogen (mol/m$^3$); $K$ is the equilibrium partition coefficient (m$^3$/mol), which can be calculated as $K = K_{\mathrm{ads}}/K_{\mathrm{des}}$. $K_{\mathrm{ads}}$ and $K_{\mathrm{des}}$ are the adsorption rate coefficient (m$^3$/s/mol) and desorption rate coefficient (1/seconds), respectively. This equation reduces to the well-known Langmuir isotherm equation in the equilibrium state when $\partial C_\mu/\partial t = 0$.

Eqs. 21 through 23 form the continuum-scale M$^3$ST model component, which simulates the transient evolution of gas pressures in the inorganic matrix and kerogen at the continuum (i.e., inch and larger) scale. Note that the gas pressure can be calculated using the gas concentration based on the ideal gas law. We developed a nonlinear finite difference solver, which used the implicit finite difference scheme and was validated in our previous publication (Chen 2016), to solve these fully coupled and nonlinear partial differential equations (Eqs. 21 through 23). The solved gas pressure in the inorganic matrix was then used to history match the evolution of gas pressures measured in the PDP experiments.

## Novel Double-Exponential Empirical Model

The microscale component of the M$^3$ST model (i.e., Eq. 19) is based on the first principles and thus provides mechanistic insight into the role of geomechanics, fluid dynamics, and Klinkenberg effect on the apparent permeability of shale. In practice, empirical correlations have been developed to describe the relation between measured permeability and effective stress. Based on the studies of Chhatre et al. (2015), King et al. (2018), and Zhu et al. (2018), the dependence of shale permeability on the variation of effective stress can be described using an exponential function. This conclusion was confirmed by the experiments from Pei et al. (2020). However, all these previous empirical correlations focused on the influence of effective stress on measured permeability, without accounting for the effect of pore pressure, which can also significantly affect laboratory-measured permeability through the Klinkenberg effect.

Based on the laboratory PDP experiments under various combinations of pore pressures and effective stresses, a novel double-exponential empirical model was proposed in this study to describe the role of both effective stress and pore pressure on the measured permeability:

$$k_a = e^{-\gamma_1(P_e - P_{e0})} \cdot \left[(k_0 - k_{a0}) \cdot e^{-\gamma_2(P_p - P_{p0})} + k_{a0}\right], \quad (24)$$

where $k_a$ is the apparent permeability (m$^2$) measured under effective stress $P_e$ and pore pressure $P_p$; $\gamma_1$ and $\gamma_2$ are the shale-permeability moduli (psi$^{-1}$) with respect to effective stress and pore pressure, respectively; $k_0$ is the reference apparent permeability (m$^2$); $P_{e0}$ and $P_{p0}$ are the reference effective stress and reference pore pressure under which $k_0$ is measured; and $k_{a0}$ is the reference absolute permeability (m$^2$) under the reference effective stress $P_{e0}$. It is clear that when the pore pressure $P_p$ is infinitely large, the Klinkenberg effect is eliminated; in this scenario, $k_a$ will be equal to $k_{a0}$ if $P_e$ is equal to $P_{e0}$.

This double-exponential empirical model will be used to fit the laboratory PDP experimental results and then compared with the M$^3$ST model fitting. In practice, the double-exponential empirical model can be used as a powerful tool to fit laboratory-measured apparent permeability under various pore pressures and effective stresses because of its simple formulation and small number of undetermined parameters (i.e., $\gamma_1$ and $\gamma_2$).

## Results and Discussion

**Table 1** illustrates the calculated values of the Biot's coefficient $\chi$ based on the PDP measurements and Eq. 8. When we calculated $\partial\log(k_a)/\mathrm{d}P_p$, the value of $P_p$ was varied, whereas the value of $P_c$ was fixed. Similarly, when we calculated $\partial\log(k_a)/\mathrm{d}P_c$, the value of $P_c$ was varied, whereas the value of $P_p$ was fixed. Particularly, we used the values of $P_p$ at 1,700, 1,800, 2,000, and 2,200 psi and fixed $P_c$ at 2,500 psi when we calculated $\partial\log(k_a)/\mathrm{d}P_p$. These relatively high $P_p$ values eliminated the Klinkenberg effect, and thus the measured apparent permeability is equal to the absolute permeability. Table 1 shows that the two core plugs from the Eagle Ford shale had Biot's coefficients less than unity, whereas the two Mancos cores had Biot's coefficients equal to unity. The Biot's coefficient in shales is critically influenced by the clay mineral content, fluid-filled pore geometries, and mineral elastic properties (Kwon et al. 2001). Because shale is well-known for its heterogeneity in mineral composition (Fan et al. 2021a), we usually treat shale as a composite material. Therefore, each shale formation has its unique petrophysical and geomechanical properties, leading to the various Biot's coefficient values in Table 1.

| | Eagle Ford 1A | Eagle Ford 1B | Mancos 1A | Mancos 1B |
|---|---|---|---|---|
| Biot's coefficient ($\chi$) | 0.60 | 0.71 | 1.0 | 1.0 |

Table 1—Measured Biot's coefficients for the four shale cores.

**Fig. 4** illustrates the PDP measurements as well as M$^3$ST model fitting and predictions. The scatter data points are PDP-measured apparent permeability values as a function of pore pressure under three effective stresses (i.e., 500, 1,000, and 1,500 psi). The effective stresses were calculated using Biot's coefficients measured in Table 1. At each effective stress, the shale's apparent permeability was measured under eight different pore pressures (i.e., 100, 300, 500, 700, 900, 1,100, 1,300, and 1,500 psi) to probe the role of the Klinkenberg effect on the measured apparent permeability. As an exception, the two Eagle Ford shale cores were measured under only the first five pore pressures at the effective stress of 500 psi because of their low Biot's coefficients, which caused the confining pressure to be comparable to the pore pressure based on Eq. 1 when the pore pressure was more than 1,000 psi. The PDP measurements used pure nitrogen at 298 K. Overall, PDP measurements in Fig. 4 show that the apparent permeability decreased with increasing pore pressure and increasing effective stress. Particularly, it was clear that the $k_a$ value did not change against pore pressure noticeably when the pore pressure value was higher than 1,300 psi because the high pore pressures can mitigate the Klinkenberg effect. This phenomenon is because a high gas pore pressure leads to a short mean-free-path length for gas molecules, which results in a small Kn and thus inhibits the Knudson diffusion. Therefore, the apparent permeability values measured less than 1,300 and 1,500 psi in Fig. 4 can be considered as the absolute permeability, which was consistent with the findings in the literature (Vermylen 2011).

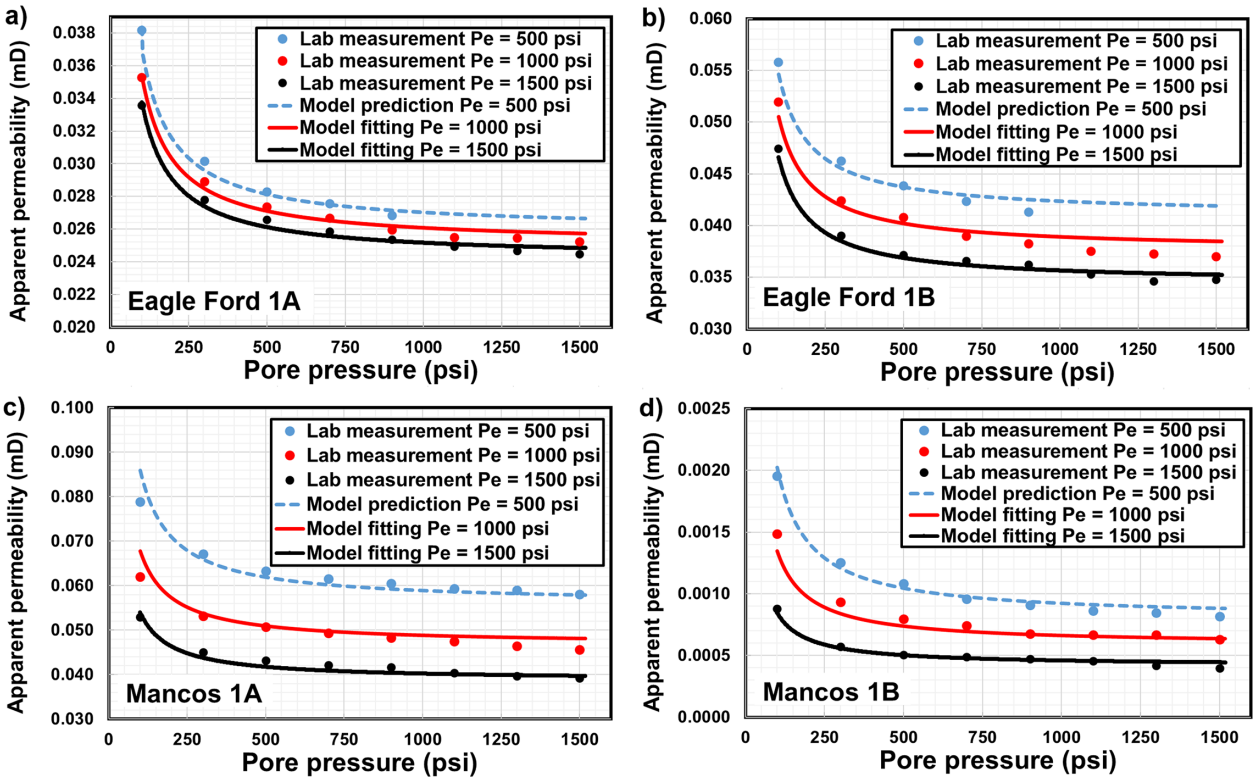

**Fig. 4—PDP-measured apparent permeability (scatter data points) as a function of pore pressure and effective stress. The solid-line curves were obtained by fitting the M$^3$ST model to the PDP measurements at $P_e$ = 1,000 and 1,500 psi based on NLSF. The dash-line curve was the M$^3$ST model prediction of the apparent permeability at $P_e$ =500 psi using the model-fitted parameters.**

Fig. 4 also illustrates the M$^3$ST model fitting and predictions. Specifically, the two solid-line curves are the fitting curves based on the M$^3$ST model, and the dash-line curve is the model prediction. Particularly, PDP-measured apparent permeability values as a function of pore pressure under effective stresses of 1,000 and 1,500 psi were fitted using the M$^3$ST model with NLSF, and the fitted parameters were then used in the model to predict the apparent permeability values under effective stress of 500 psi. **Table 2** demonstrates the six unknown parameters in the M$^3$ST model that were determined by fitting experimental PDP data. In this study, the Gauss-Newton method, an iteration-based algorithm for solving NLSF problems, was used to determine the six unknown parameters in the M$^3$ST model through data fitting. Particularly, the vector of the unknown parameters **β**, which has six elements in this case, is calculated by

$$\boldsymbol{\beta}^{n+1} = \boldsymbol{\beta}^{n} + \left(\mathbf{J}^T\mathbf{J}\right)^{-1}\mathbf{J}^T\mathbf{r}, \quad (25)$$

where $n$ indicates the iteration timestep; **J** is the Jacobian matrix, in which each entry $J_{ij}$ is the derivative of the M$^3$ST-predicted $k_\mathrm{a}$ value (i.e., based on Eq. 19) with respect to the $j$th unknown parameter at the $i$th measurement; **r** is the residual vector, in which each element $r_i$ is the difference between the PDP-measured and model-predicted $k_\mathrm{a}$ values at the $i$th measurement.

| Parameter | Eagle Ford 1A | Eagle Ford 1B | Mancos 1A | Mancos 1B |
|---|---|---|---|---|
| $S$ (m) | $5.25\times10^{-4}$ | $5.17\times10^{-4}$ | $1.12\times10^{-4}$ | $9.07\times10^{-4}$ |
| $h_{i0}$ (m) | $5.53\times10^{-7}$ | $6.74\times10^{-7}$ | $4.73\times10^{-7}$ | $2.51\times10^{-7}$ |
| $h_{k0}$ (m) | $1.80\times10^{-10}$ | $5.90\times10^{-9}$ | $5.62\times10^{-10}$ | $6.57\times10^{-10}$ |
| $N$ | $1.0\times10^{3}$ | $1.0\times10^{2}$ | $1.0\times10^{3}$ | $1.0\times10^{3}$ |
| $\beta_i$ (Pa$^{-1}$) | $3.2\times10^{-9}$ | $8.2\times10^{-9}$ | $2.8\times10^{-8}$ | $4.3\times10^{-8}$ |
| $\beta_k$ (Pa$^{-1}$) | $1.8\times10^{-8}$ | $6.7\times10^{-9}$ | $5.0\times10^{-8}$ | $5.5\times10^{-8}$ |

Table 2—Parameter values determined by fitting the M$^3$ST model to the laboratory PDP measurements at effective stresses of 1,000 and 1,500 psi using NLSF based on the Gauss-Newton method.

Using the Gauss-Newton method, we used the determined parameters, based on fitting the microscale M$^3$ST model component to the PDP-measured data under effective stresses of 1,000 and 1,500 psi to predict the apparent permeability as a function of pore pressure under effective stress of 500 psi. **Table 3** demonstrates the accuracy of the M$^3$ST model predictions for effective stress of 500 psi. We evaluated the difference between PDP-measured and model-predicted $k_\mathrm{a}$ values using the normalized mean squared error (NMSE), which is defined as

$$\mathrm{NMSE}(k_a, \hat{k}_a) = \frac{\sum_{i=1}^{N}\left(k_{ai} - \hat{k}_{ai}\right)^2}{\sum_{i=1}^{N} {k_{ai}}^2}, \quad (26)$$

where $k_{ai}$ is the $i$th PDP measurement of apparent permeability, $\hat{k}_{ai}$ is the corresponding prediction using the M$^3$ST model, and $N$ is the total number of measurements. The NMSE is a measure to evaluate the relative error of model predictions compared to experimental observations. The smaller the NMSE value, the lower the relative error. The parameters fitted using the measurements under effective stresses of 1,000 and 1,500 psi led to accurate predictions of apparent permeability as a function of pore pressure under the effective stress of 500 psi for all four shale samples. This NMSE result indicates that the microscale M$^3$ST model component successfully accounted for the mechanistic, multiphysics mechanisms that regulate shale's apparent permeability in the steady state.

| $P_e$ | Eagle Ford 1A | Eagle Ford 1B | Mancos 1A | Mancos 1B |
|---|---|---|---|---|
| 500 psi | $7.85\times10^{-5}$ | $3.47\times10^{-4}$ | $1.69\times10^{-3}$ | $1.73\times10^{-3}$ |

Table 3—NMSE values for M$^3$ST model predictions of shale's apparent permeability under effective stress of 500 psi.

**Fig. 5** illustrates the laboratory PDP measurements as well as the double-exponential empirical model (i.e., Eq. 24 fitting based on NLSF for all four shale core samples). The data point at $P_e = 500$ psi and $P_p = 100$ psi was selected as the reference point, so $P_{e0}$ and $P_{p0}$ were 500 and 100 psi, respectively. $k_0$ was the PDP-measured apparent permeability at the reference point. $k_{a0}$ was the absolute permeability when $P_e = 500$ psi (i.e., stable value of apparent permeability at the right end of the blue solid lines in Fig. 5). The double-exponential empirical model can overall capture the apparent permeability variation as a function of both pore pressure and effective stress.

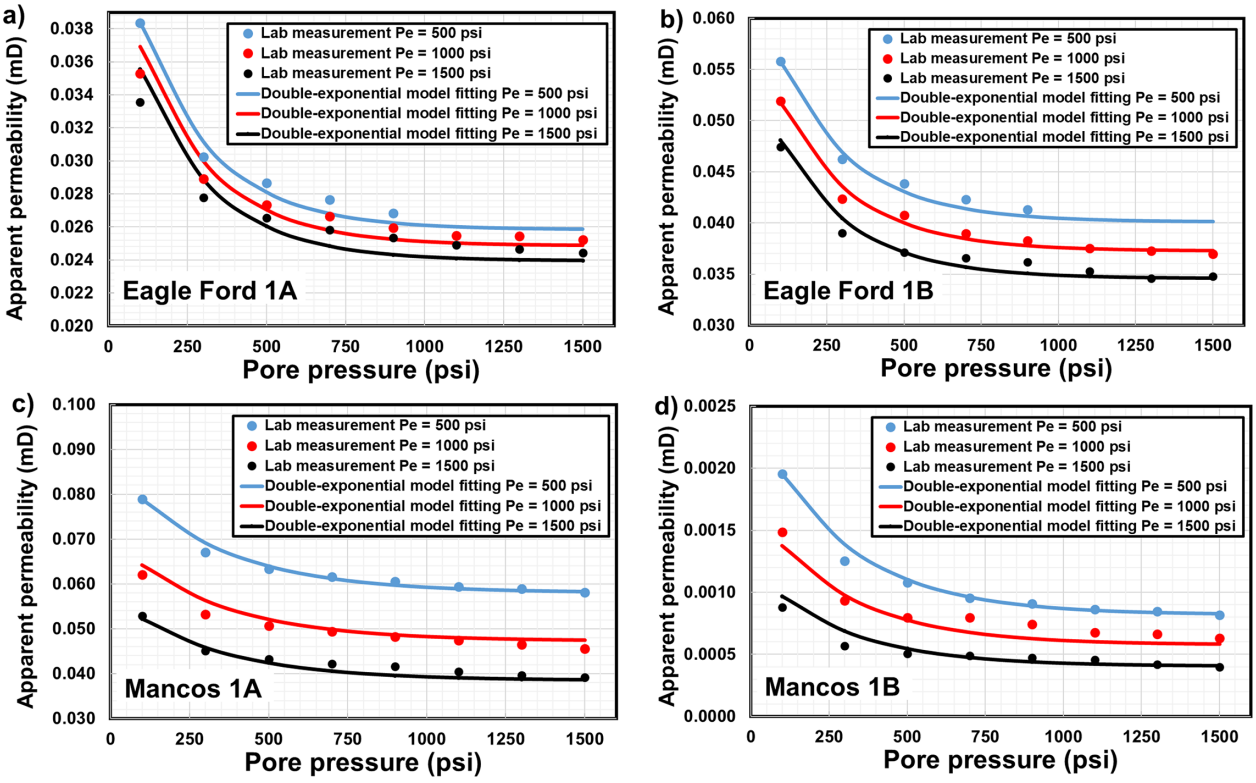


**Fig. 5—PDP-measured apparent permeability (scatter data points) as a function of pore pressure and effective stress. The solid-line curves were obtained by fitting the double-exponential empirical model to the PDP measurements based on NLSF.**

**Table 4** demonstrates the comparison of the NMSE values for global data fitting using the M$^3$ST model (i.e., Eq. 19) and the double-exponential empirical model (i.e., Eq. 24). Global data fitting means that the model was used to fit all the laboratory PDP measurements under effective stresses of 500, 1,000, and 1,500 psi. Therefore, the NMSE value was calculated based on the experimental measurements under all the effective stresses. Table 4 shows that the NMSE measures of the M$^3$ST global data fitting were overall lower than those for the global data fitting using the empirical model, which confirms that the M$^3$ST model was based on the first principles and thus successfully accounted for the mechanistic, multiphysics processes that regulate shale's apparent permeability under various combinations of pore pressures and effective stresses.

| Sample | NMSE of M$^3$ST Global Fitting | NMSE of Empirical Model Global Fitting |
|---|---|---|
| Eagle Ford 1 A | $1.27\times10^{-4}$ | $1.10\times10^{-3}$ |
| Eagle Ford 1B | $2.18\times10^{-4}$ | $3.04\times10^{-4}$ |
| Mancos 1 A | $1.13\times10^{-3}$ | $6.32\times10^{-4}$ |
| Mancos 1B | $4.24\times10^{-3}$ | $6.60\times10^{-3}$ |

Table 4—NMSE values for global fitting using the M$^3$ST model and the double-exponential empirical model.

In practice, however, the double-exponential empirical model has some advantages because of its simplicity. **Table 5** illustrates the modulus values in Eq. 24, determined by fitting all the laboratory PDP measurements using NLSF based on the Gauss-Newton method. The values of $\gamma_2$ were in general higher than those of $\gamma_1$. This implies that the pore pressure influenced shale's apparent permeability more noticeably than effective stress in the current range of pore pressure. The double-exponential empirical model can be used as a powerful alternative to the M$^3$ST model to fit laboratory-measured apparent permeability under various pore pressures and effective stresses because of its simple formulation and small number of undetermined parameters.

| Sample | $\gamma_1$ (psi$^{-1}$) | $\gamma_2$ (psi$^{-1}$) |
|---|---|---|
| Eagle Ford 1 A | $7.61\times10^{-5}$ | $4.30\times10^{-3}$ |
| Eagle Ford 1B | $1.49\times10^{-4}$ | $4.10\times10^{-3}$ |
| Mancos 1 A | $4.12\times10^{-4}$ | $3.10\times10^{-3}$ |
| Mancos 1B | $7.03\times10^{-4}$ | $3.40\times10^{-3}$ |

Table 5—Fitted values of $\gamma_1$ and $\gamma_2$ in the double-exponential empirical model.

The fitted parameters in the microscale M$^3$ST model component (Eq. 19) were used to calculate the apparent permeabilities of kerogen and inorganic matrix based on Eq. 20, which were then imported into the continuum-scale M$^3$ST model component (i.e., Eqs. 21 through 23) for large-scale, transient-state simulations of gas pressure evolutions in the core. Other known parameter values used in the continuum-scale M$^3$ST model component were $C_{\mu\max} = 1800\,\text{mol/m}^3$, $\text{K} = 1.7\times10^{-4}\,\text{m}^3/\text{mol}$, $K_{\text{des}} = 1.4\times10^{-7}\,\text{s}^{-1}$, $M = 0.028\,\text{kg/mol}$, $m = 3.0\times10^{-6}\,\text{s}^{-1}$, $T = 298\,\text{K}$, and $\mu = 1.75\times10^{-5}\,\text{Pa·s}$. We used these parameter values from previous studies (Pribylov et al. 2014; Chen 2016) because the variations of these parameter values did not noticeably affect the numerical model output at the experimental time scale, which was dominated by the apparent permeability of the inorganic matrix $k_{ai}$, because viscous flow in the inorganic matrix was the dominant mechanism that regulated core-scale pressure evolutions at the time scale of interest. **Fig. 6** illustrates the transient-state M$^3$ST simulations that were used to history match the PDP-measured upstream and downstream gas pressure evolutions. Experimental conditions used in the laboratory PDP measurements are shown in **Table 6.** Particularly, the values of downstream gas pressure $P_d$ and pressure difference $\Delta P$ were experimental readings from the pressure transducers. The confining pressure in these PDP measurements was fixed at 1,500 psi. In the continuum-scale simulations, the pore pressure in each gridblock was solved in each timestep using the implicit finite difference scheme, and then the effective stress in each gridblock was determined using Eq. 1. Therefore, the pore pressure and effective stress in each gridblock continuously changed. Consequently, the kerogen permeability and inorganic matrix permeability of each gridblock were updated in each timestep using the updated pore pressure and effective stress values based on Eq. 20. However, it should be noted that the variations of kerogen permeability and inorganic matrix permeability were minimal because the value of $\Delta P$ was much lower than that of $P_d$. In practice, we only needed to make minor adjustments on $h_{i0}$, $h_{k0}$, $\beta_i$, and $\beta_k$ based on their fitted values shown in Table 2 to match the simulated pressures to the PDP-measured pressures. Overall, the continuum-scale M$^3$ST simulations managed to history match the PDP-measured evolutions of upstream and downstream gas pressures. This indicates that the kerogen and inorganic matrix permeabilities, determined through the microscale M$^3$ST-model-fitted parameters, can successfully match the laboratory PDP experimental data using large-scale, transient-state pressure predictions based on the continuum-scale M$^3$ST model component (i.e., Eqs. 21 through 23). This suggests that the M$^3$ST model is able to account for the dominant mechanisms that regulate geomechanics and gas flow at both the microscopic and continuum scales.

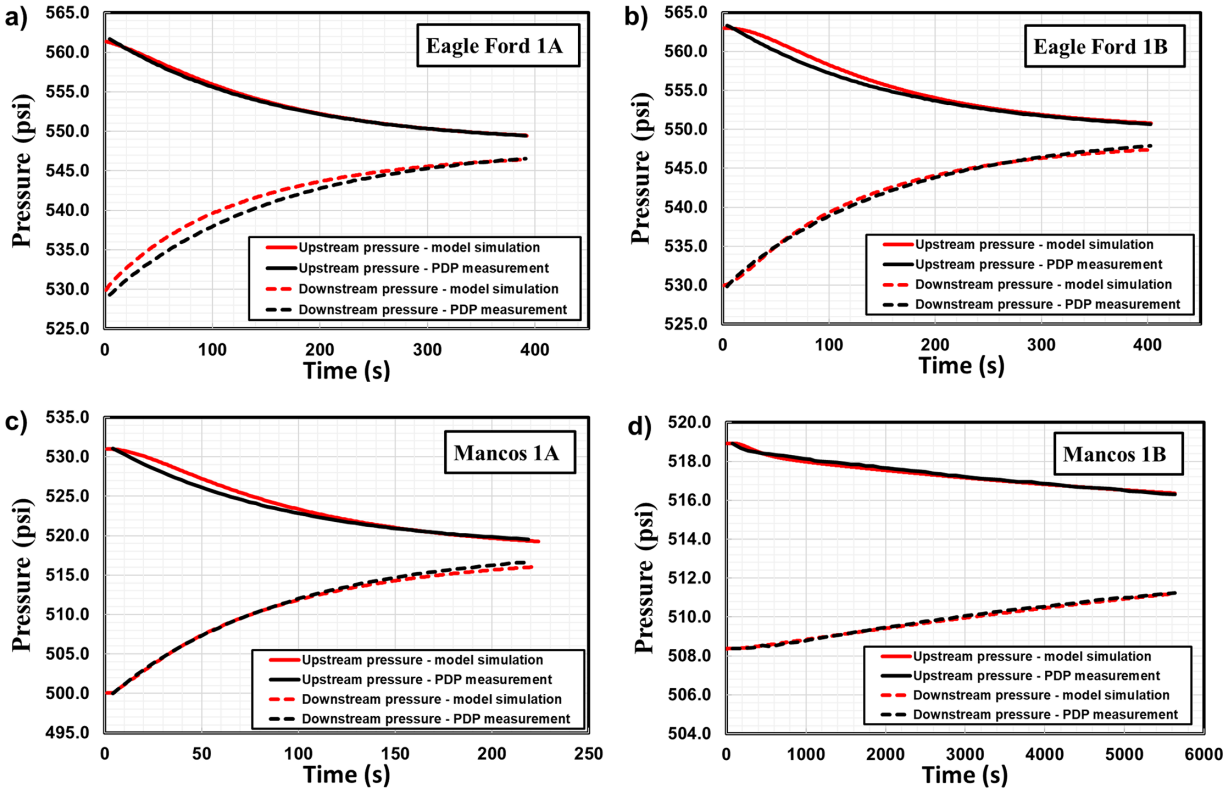


**Fig. 6—History matching of PDP-measured upstream and downstream gas pressures using the continuum-scale M$^3$ST model component.**

| Parameter | Eagle Ford 1A | Eagle Ford 1B | Mancos 1A | Mancos 1B |
|---|---|---|---|---|
| Initial $\Delta P$ (psi) | 32.4 | 33.4 | 31.0 | 10.5 |
| Initial $P_u$ (psi) | 561.7 | 563.3 | 531.0 | 518.9 |
| Initial $P_d$ (psi) | 529.3 | 529.9 | 500.0 | 508.4 |

Table 6—Experimental conditions in PDP measurements. $P_u$ and $P_d$ are gas pressures in the upstream and downstream reservoirs, respectively. $\Delta P$ is the difference between $P_u$ and $P_d$.

**Fig. 7** illustrates a sensitivity analysis that studied the effect of the apparent permeability of the inorganic matrix $k_{ai}$ on upstream and downstream pressure evolutions, which were simulated using the continuum-scale M$^3$ST model component. Three values of $k_{ai}$ were used in this sensitivity analysis, including $1\times10^{-2}$, $1\times10^{-3}$, and $1\times10^{-4}$ md. The sensitivity analysis demonstrated that the value of $k_{ai}$ significantly influenced the variations of the upstream and downstream gas pressures. A high value of $k_{ai}$ (e.g., $1\times10^{-2}$ md) resulted in relatively fast variations of the upstream and downstream gas pressures, leading to a rapid decay rate of the pressure difference. It was also noticed that the evolutions of upstream and downstream gas pressures were relatively insensitive to other parameters in the continuum-scale M$^3$ST model component. This is because in a shale core plug the overall apparent permeability is primarily contributed by the inorganic pores, and thus a higher inorganic permeability is favorable for faster gas molecule migration from the upstream end to the downstream end, leading to a faster decay rate of the pressure difference.

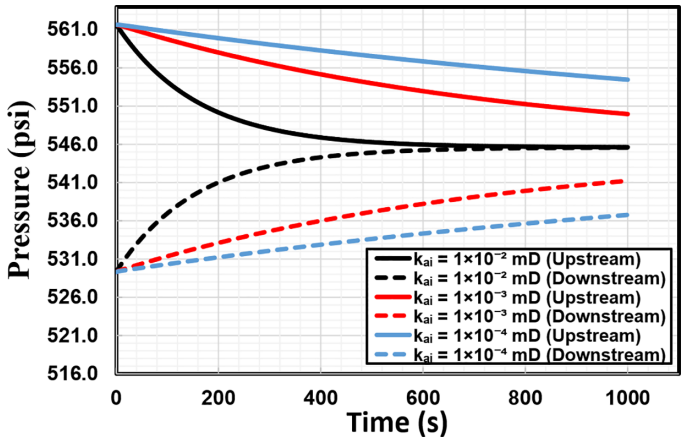


**Fig. 7—Impact of the apparent permeability of inorganic matrix $k_{ai}$ on upstream and downstream gas pressure evolutions.**

## Conclusions

A novel M$^3$ST model was developed to investigate gas transport in shales in both steady and transient states using experimental and modeling approaches. The microscale M$^3$ST model component contains a kerogen domain and an inorganic matrix domain, both of which are subjected to confining stress. Each domain has its respective geomechanical and gas transport properties. We used a laboratory PDP to measure the permeabilities of various shale cores to calibrate the microscale M$^3$ST model component and to quantify the parameters in the steady state. We used the microscale M$^3$ST model component to fit the PDP-measured apparent permeability as a function of pore pressure under two effective stresses based on NLSF, and the fitted model parameters were able to provide accurate model predictions for other effective stresses. We then imported the parameters and petrophysical properties determined in the steady state into the transient-state, continuum-scale M$^3$ST model component, which performed history matching of the evolutions of the upstream and downstream gas pressures as a function of time at the core scale. In addition, we introduced a double-exponential empirical model, which is a powerful alternative to the M$^3$ST model to fit laboratory-measured apparent permeability under various pore pressures and effectives stresses because of its simple formulation and small number of undetermined parameters. The M$^3$ST model and the research findings in this study provided critical insights into the role of the multiphysics mechanisms, including geomechanics, fluid dynamics and transport, and the Klinkenberg effect on the transport of shale gas across different spatial scales in both steady and transient states.

## Nomenclature

$A$ = model total cross-sectional area, m$^2$
$A_i$ = inorganic matrix cross-sectional area, m$^2$
$\mathbf{A_k}$ = kerogen cross-sectional area, m$^2$
$b$ = Klinkenberg coefficient, Pa
$b_i$ = Klinkenberg coefficient of inorganic matrix, Pa
$b_k$ = Klinkenberg coefficient of kerogen, Pa
$C_i$ = molar concentration of free gas within the inorganic matrix, mol/m$^3$
$C_k$ = molar concentration of free gas within the kerogen, mol/m$^3$
$C_\mu$ = adsorbed gas molar concentration within kerogen, mol/m$^3$
$C_{\mu\max}$ = maximum monolayer adsorption of gas molar concentration within kerogen, mol/m$^3$
$h$ = effective pore width, m
$h_i$ = effective pore width in inorganic matrix, m
$h_{i0}$ = reference pore width in inorganic matrix, m
$h_k$ = effective pore width in kerogen, m

$h_{k0}$ = reference pore width in kerogen, m
$k$ = absolute permeability, $m^2$
$k_a$ = apparent permeability, $m^2$
$k_{a0}$ = reference absolute permeability, $m^2$
$\overline{k_a}$ = overall apparent permeability, $m^2$
$k_{ai}$ = apparent permeability of inorganic matrix, $m^2$
$k_{ak}$ = apparent permeability of kerogen, $m^2$
$k_{ap}$ = model-predicted apparent permeability, $m^2$
$k_0$ = reference measured permeability, $m^2$
$K$ = equilibrium partition coefficient, $m^3$/mol
$K_{ads}$ = adsorption rate coefficient, $m^3$/s/mol
$K_{des}$ = desorption rate coefficient, 1/s
$m$ = mass-exchange-rate coefficient, 1/s
$M$ = molar mass, kg/mol
$N$ = number ratio
$P_c$ = confining pressure, Pa
$P_d$ = downstream pressure of measured sample, Pa
$P_e$ = effective stress, Pa
$P_p$ = pore pressure, Pa
$P_u$ = upstream pressure of measured sample, Pa
$Q_i$ = flow rate in the inorganic matrix, $m^3$/s
$Q_k$ = flow rate in the kerogen, $m^3$/s
$R$ = gas constant, J/mol/K
$S$ = model solid cross-sectional area, $m^2$
$t$ = running time, seconds
$T$ = absolute temperature, K
$x$ = distance in the core longitudinal direction, m
$z$ = compressibility factor
$\alpha$ = tangential momentum accommodation coefficient
$\beta_i$ = compressibility of inorganic matrix, 1/Pa
$\beta_k$ = compressibility of kerogen, 1/Pa
$\gamma_1$ = permeability modulus for effective stress, 1/psi
$\gamma_2$ = permeability modulus for pore pressure, 1/psi
$\Gamma$ = mass transfer rate between kerogen and inorganic matrix, mol/$m^3$/s
$\Delta P$ = differential pressure in the PDP measurement, Pa
$\varepsilon_{kp}$ = kerogen pore volume per unit total pore volume
$\varepsilon_{ks}$ = kerogen solid volume per unit total solid volume
$\lambda$ = free gas mean-free-path length, m
$\mu$ = dynamic viscosity, Pa·s
$\rho$ = free gas mass density, Pa·s
$\phi$ = total porosity
$\chi$ = Biot's coefficient

## Acknowledgments

We acknowledge the funding support from the American Chemical Society Petroleum Research Fund (ACS-PRF) under the award number of 60105-ND9 and the funding support from the US Department of Energy through the National Energy Technology Laboratory under Contract No. DE-FE0031576.

## Reference

Akkutlu, I. Y. and Fathi, E. 2012. Multiscale Gas Transport in Shales with Local Kerogen Heterogeneities. *SPE J.* **17** (4): 1002–1011. SPE-146422-PA. https://doi.org/10.2118/146422-PA.

Alnoaimi, K. R. and Kovscek, A. R. 2013. Experimental and Numerical Analysis of Gas Transport in Shale Including the Role of Sorption. Paper presented at the SPE Annual Technical Conference and Exhibition, New Orleans, Louisiana, USA, 30 September–2 October. SPE-166375-MS. https://doi.org/10.2118/166375-MS.

Bernabe, Y. 1986. The Effective Pressure Law for Permeability in Chelmsford Granite and Barre Granite. *Int J Rock Mech Min Sci Geomech Abstr* **23** (3): 267–275. https://doi.org/10.1016/0148-9062(86)90972-1.

Beskok, A. and Karniadakis, G. E. 1999. A Model for Flows in Channels, Pipes, and Ducts at Micro and Nano Scales. *Nanosc Microsc Therm* **3** (1): 43–77. https://doi.org/10.1080/108939599199864.

Biot, M. A. 1941. General Theory of Three-Dimensional Consolidation. *J Appl Phys* **12** (2): 155–164. https://doi.org/10.1063/1.1712886.

Blanchard, V., Lasseux, D., Bertin, H. J. et al. 2007. Gas/Water Flow in Porous Media in the Presence of Adsorbed Polymer: Experimental Study on Non-Darcy Effects. *SPE Res Eval & Eng* **10** (4): 423–431. SPE-99711-PA. https://doi.org/10.2118/99711-PA.

Chen, C. 2016. Multiscale Imaging, Modeling, and Principal Component Analysis of Gas Transport in Shale Reservoirs. *Fuel* **182:** 761–770. http://doi.org/10.1016/j.fuel.2016.06.020.

Chen, C., Hu, D., Westacott, D. et al. 2013. Nanometer-Scale Characterization of Microscopic Pores in Shale Kerogen by Image Analysis and Pore-Scale Modeling. *Geochem Geophy Geosyst* **14** (10): 4066–4075. https://doi.org/10.1002/ggge.20254.

Chen, C. and Zeng, L. 2015. Using the Level Set Method To Study the Effects of Heterogeneity and Anisotropy on Hyporheic Exchange. *Water Resour Res* **51** (5): 3617–3634. http://doi.org/10.1002/2014wr016444.

Cheng, A. D. 1997. Material Coefficients of Anisotropic Poroelasticity. *Int J Rock Mech Min Sci* **34** (2): 199–205. https://doi.org/10.1016/S0148-9062(96)00055-1.

Chhatre, S. S., Braun, E. M., Sinha, S. et al. 2015. Steady-State Stress-Dependent Permeability Measurements of Tight Oil-Bearing Rocks. *Petrophysics* **56** (2): 116–124. SPWLA-2015-v56n2a2.

Civan, F. 2020. Can Moderately Rarefied Gas Transport through Round and Flat Tight Channels of Fractured Porous Media Be Described Accurately? *Transport Porous Med* **132** (1): 157–181. https://doi.org/10.1007/s11242-020-01385-1.

Civan, F. 2021. Effective-Stress Coefficients of Porous Rocks Involving Shocks and Loading/Unloading Hysteresis. *SPE J*. **26** (1): 44–67. SPE-200501-PA. https://doi.org/10.2118/200501-PA.

Dicker, A. I. and Smits, R. M. 1988. Practical Approach for Determining Permeability from Laboratory Pressure-Pulse Decay Measurements. Paper presented at the SPE International Meeting on Petroleum Engineering, Tianjin, China, 1–4 November. SPE-17578-MS. https://doi.org/10.2118/17578-MS.

Fan, M., Han, Y., Tan, X. et al. 2021a. Experimental and Numerical Characterization of Lower Huron Shale as a Heterogeneous Material. *Rock Mech Rock Eng* **54**: 4183–4200. https://doi.org/10.1007/s00603-021-02491-2.

Fan, M., Li, Z., Han, Y. et al. 2021b. Experimental and Numerical Investigations of the Role of Proppant Embedment on Fracture Conductivity in Narrow Fractures. *SPE J*. **26** (1): 324–341. SPE-204222-PA. https://doi.org/10.2118/204222-PA.

Fan, M., McClure, J., Han, Y. et al. 2018. Interaction between Proppant Compaction and Single-/Multiphase Flows in a Hydraulic Fracture. *SPE J*. **23** (4): 1290–1303. SPE-189985-PA. https://doi.org/10.2118/189985-PA.

Geertsma, J. 1957. The Effect of Fluid Pressure Decline on Volumetric Changes of Porous Rocks. In *Transactions of the Society of Petroleum Engineers*, Vol. 210, Issue 1, SPE-728-G, 331–340. Richardson, Texas, USA: Society of Petroleum Engineers. https://doi.org/10.2118/728-G.

Ghanbarian, B. and Javadpour, F. 2017. Upscaling Pore Pressure-Dependent Gas Permeability in Shales. *J Geophys Res Solid Earth* **122** (4): 2541–2552. https://doi.org/10.1002/2016JB013846.

Gu, M. and Mohanty, K. K. 2014. Effect of Foam Quality on Effectiveness of Hydraulic Fracturing in Shales. *Int J Rock Mech Min Sci* **70:** 273–285. https://doi.org/10.1016/j.ijrmms.2014.05.013.

Guo, R., Dalton, L. E., Fan, M. et al. 2020. The Role of the Spatial Heterogeneity and Correlation Length of Surface Wettability on Two-Phase Flow in a $CO_2$-Water-Rock System. *Adv Water Resour* **146:** 103763. https://doi.org/10.1016/j.advwatres.2020.103763.

Guo, B., Ma, L., and Tchelepi, H. A. 2018. Image-Based Micro-Continuum Model for Gas Flow in Organic-Rich Shale Rock. *Adv Water Resour* **122:** 70–84. https://doi.org/10.1016/j.advwatres.2018.10.004.

Hayek, M. 2015. Exact Solutions for One-Dimensional Transient Gas Flow in Porous Media with Gravity and Klinkenberg Effects. *Transport Porous Med* **107** (2): 403–417. https://doi.org/10.1007/s11242-014-0445-x.

Heller, R., Vermylen, J., and Zoback, M. 2014. Experimental Investigation of Matrix Permeability of Gas Shales. *AAPG Bull* **98** (5): 975–995. https://doi.org/10.1306/09231313023.

Hu, G., Wang, H., Fan, X. et al. 2009. Mathematical Model of Coalbed Gas Flow with Klinkenberg Effects in Multi-Physical Fields and Its Analytic Solution. *Transport Porous Med* **76** (3): 407–420. https://doi.org/10.1007/s11242-008-9254-4.

Innocentini, M. D. and Pandolfelli, V. C. 2001. Permeability of Porous Ceramics considering the Klinkenberg and Inertial Effects. *J Am Ceram Soc* **84** (5): 941–944. https://doi.org/10.1111/j.1151-2916.2001.tb00772.x.

Jones, S. C. 1997. A Technique for Faster Pulse-Decay Permeability Measurements in Tight Rocks. *SPE Form Eval* **12** (1): 19–26. SPE-28450-PA. https://doi.org/10.2118/28450-PA.

King, H., Sansone, M., Kortunov, P. et al. 2018. Microstructural Investigation of Stress-Dependent Permeability in Tight-Oil Rocks. *Petrophysics* **59** (1): 35–43. SPWLA-2018-v59n1a3.

Klinkenberg, L. J. 1941. The Permeability of Porous Media to Liquids and Gases. Paper presented at the Drilling and Production Practice, New York, New York, USA, 1 January. API-41-200.

Kwon, O., Kronenberg, A. K., Gangi, A. F. et al. 2001. Permeability of Wilcox Shale and Its Effective Pressure Law. *J Geophys Res Solid Earth* **106** (B9): 19339–19353. https://doi.org/10.1029/2001JB000273.

Lee, M. W. 2002. Biot-Gassmann Theory for Velocities of Gas Hydrate-Bearing Sediments. *Geophysics* **67** (6): 1711–1719. https://doi.org/10.1190/1.1527072.

Li, Z., Ripepi, N., and Chen, C. 2019. Comprehensive Laboratory Investigation and Model Fitting of Klinkenberg Effect and Its Role on Apparent Permeability in Various US Shale Formations. Paper presented at the 53rd US Rock Mechanics/Geomechanics Symposium, New York, New York, USA, 23–26 June. ARMA-2019-1568.

Li, Z., Ripepi, N., and Chen, C. 2020. Using Pressure Pulse Decay Experiments and a Novel Multi-Physics Shale Transport Model To Study the Role of Klinkenberg Effect and Effective Stress on the Apparent Permeability of Shales. *J Pet Sci Eng* **189:** 107010. https://doi.org/10.1016/j.petrol.2020.107010.

Li, C., Xu, P., Qiu, S. et al. 2016a. The Gas Effective Permeability of Porous Media with Klinkenberg Effect. *J Nat Gas Sci Eng* **34:** 534–540. https://doi.org/10.1016/j.jngse.2016.07.017.

Li, Z., Zhang, W., Tang, Y. et al. 2016b. Formation Damage During Alkaline-Surfactant-Polymer Flooding in the Sanan-5 block of the Daqing Oilfield, China. *J Nat Gas Sci Eng* **35:** 826–835. https://doi.org/10.1016/j.jngse.2016.07.046.

Mehmani, A., Prodanović, M., and Javadpour, F. 2013. Multiscale, Multiphysics Network Modeling of Shale Matrix Gas Flows. *Transport Porous Med* **99** (2): 377–390. https://doi.org/10.1007/s11242-013-0191-5.

Montgomery, C. T. and Smith, M. B. 2010. Hydraulic Fracturing: History of an Enduring Technology. *J Pet Technol* **62** (12): 26–40. SPE-1210-0026-JPT. https://doi.org/10.2118/1210-0026-JPT.

Müller, T. and Sahay, P. 2016. Biot Coefficient is Distinct from Effective Pressure Coefficient. *Geophysics* **81** (4): L27–L33. https://doi.org/10.1190/geo2015-0625.1.

Ojala, I. O. and Fjær, E. 2007. The Effective Stress Coefficient in Porous Sandstone. Paper presented at the 1st Canada-US Rock Mechanics Symposium, Vancouver, Canada, ARMA-07-101.

Pei, Y., Yu, W., Sepehrnoori, K. et al. 2020. The Influence of Development Target Depletion on Stress Evolution and Well Completion of Upside Target in the Permian Basin. Paper presented at the SPE/AAPG/SEG Unconventional Resources Technology Conference, Virtual, 20–22 July. URTEC-2020-3110. https://doi.org/10.15530/urtec-2020-3110.

Pribylov, A. A., Skibitskaya, N. A., and Zekel', L. A. 2014. Sorption of Methane, Ethane, Propane, Butane, Carbon Dioxide, and Nitrogen on Kerogen. *Russ J Phys Chem* **88** (6): 1028–1036. https://doi.org/10.1134/S0036024414060259.

Selvadurai, A. P. S. 2019. The Biot Coefficient for a Low Permeability Heterogeneous Limestone. *Continuum Mech Therm* **31** (4): 939–953. https://doi.org/10.1007/s00161-018-0653-7.

Sheng, G., Javadpour, F., and Su, Y. 2018. Effect of Microscale Compressibility on Apparent Porosity and Permeability in Shale Gas Reservoirs. *Int J Heat Mass Tran* **120:** 56–65. https://doi.org/10.1016/j.ijheatmasstransfer.2017.12.014.

Soeder, D. J. 1988. Porosity and Permeability of Eastern Devonian Gas Shale. *SPE Form Eval* **3** (1): 116–124. SPE-15213-PA. https://doi.org/10.2118/15213-PA.

Stringfellow, W. T., Domen, J. K., Camarillo, M. K. et al. 2014. Physical, Chemical, and Biological Characteristics of Compounds Used in Hydraulic Fracturing. *J Hazard Mater* **275:** 37–54. https://doi.org/10.1016/j.jhazmat.2014.04.040.

Tan, X. and Konietzky, H. 2014. Numerical Study of Variation in Biot's Coefficient with Respect to Microstructure of Rocks. *Tectonophysics* **610:** 159–171. https://doi.org/10.1016/j.tecto.2013.11.014.

Tang, Y., Wang, R., Li, Z. et al. 2019. Experimental Study on Spontaneous Imbibition of $CO_2$-Rich Brine in Tight Oil Reservoirs. *Energy Fuels* **33** (8): 7604–7613. https://doi.org/10.1021/acs.energyfuels.9b01621.

Terzaghi, K., Peck, R. B., and Mesri, G. 1996. *Soil Mechanics in Engineering Practice*. New York, New York, USA: John Wiley & Sons.

Tian, Y., Yu, X., Li, J. et al. 2019. Scaling Law for Slip Flow of Gases in Nanoporous Media from Nanofluidics, Rocks, and Pore-Scale Simulations. *Fuel* **236:** 1065–1077. https://doi.org/10.3997/2214-4609.201802220.

Vermylen, J. P. 2011. *Geomechanical Studies of the Barnett Shale*, *Texas*. PhD dissertation, Stanford University, Stanford, California, USA (May 2011).

Wang, Q., Hu, Y., Zhao, J. et al. 2019. Multiscale Apparent Permeability Model of Shale Nanopores Based on Fractal Theory. *Energies* **12** (17): 3381. https://doi.org/10.3390/en12173381.

Wang, H., Rabiei, M., Lei, G. et al. 2017. A Novel Granular Profile Control Agent for Steam Flooding: Synthesis and Evaluation. Paper presented at the SPE Western Regional Meeting, Bakersfield, California, USA, 23–27 April. SPE-185650-MS. https://doi.org/10.2118/185650-MS.

Wang, H., Rabiei, M., Wang, S. et al. 2018. Fracture Quantification Method with 3D X-Ray Image-Entropy-Assisted Indicator Kriging Method. Paper presented at the SPE Western Regional Meeting, Garden Grove, California, USA. 22–26 April. SPE-190045-MS. https://doi.org/10.2118/190045-MS.

Wang, G., Ren, T., Wang, K. et al. 2014. Improved Apparent Permeability Models of Gas Flow in Coal with Klinkenberg Effect. *Fuel* **128:** 53–61. https://doi.org/10.1016/j.fuel.2014.02.066.

Warpinski, N. R. and Teufel, L. W. 1992. Determination of the Effective-Stress Law for Permeability and Deformation in Low-Permeability Rocks. *SPE Form Eval* **7** (2): 123–131. SPE-20572-PA. https://doi.org/10.2118/20572-PA.

Wu, Y., Pruess, K., and Persoff, P. 1998. Gas Flow in Porous Media with Klinkenberg Effects. *Transport Porous Med* **32** (1): 117–137. https://doi.org/10.1023/A:1006535211684.

Yuan, Q., Mehmani, Y., Burnham, A. K. et al. 2020. Scaling Analysis of the Coupled Compaction, Kerogen Conversion, and Petroleum Expulsion during Geological Maturation. *J Pet Sci Eng* **192:** 107285. https://doi.org/10.1016/j.petrol.2020.107285.

Zhang, Q., Yan, X., and Shao, J. 2021. Fluid Flow through Anisotropic and Deformable Double Porosity Media with Ultra-Low Matrix Permeability: A Continuum Framework. *J Pet Sci Eng* **200:** 108349. https://doi.org/10.1016/j.petrol.2021.108349.

Zhao, F., Li, Z., Wu, J. et al. 2017. New Type Plugging Particle System with High Temperature & High Salinity Resistance. *J Pet Sci Eng* **152:** 317–329. https://doi.org/10.1016/j.petrol.2017.03.024.

Zhao, Q., Zhu, J., Cao, G. et al. 2021. Transient Modeling of Plunger Lift for Gas Well Deliquification. *SPE J*. 1–20. SPE-205386-PA. https://doi.org/10.2118/205386-PA.

Zhu, S. Y., Du, Z. M., Li, C. L. et al. 2018. A Semi-Analytical Model for Pressure-Dependent Permeability of Tight Sandstone Reservoirs. *Transport Porous Med* **122** (2): 235–252. https://doi.org/10.1007/s11242-018-1001-x.

Zhu, W. C., Liu, J., Sheng, J. C. et al. 2007. Analysis of Coupled Gas Flow and Deformation Process with Desorption and Klinkenberg Effects in Coal Seams. *Int J Rock Mech Min Sci* **44** (7): 971–980. https://doi.org/10.1016/j.ijrmms.2006.11.008.